

# PROCEEDINGS OF SPIE

[SPIDigitalLibrary.org/conference-proceedings-of-spie](https://spiedigitallibrary.org/conference-proceedings-of-spie)

## SUBARU prime focus spectrograph integration and performance at LAM

Madec, F., Pascal, S., Le Fur, A., Le Mignant, D., Dohlen, K., et al.

F. Madec, S. Pascal, A. Le Fur, D. Le Mignant, K. Dohlen, R. Barette, M. Belhadi, S. Smee, J. Gunn, J. Le Merrer, M. Llored, M. Jaquet, P. Balard, P. Blanchard, F. Roman, V. Lapere, J. F. Gabriel, C. Loomis, M. Golebiowski, M. Hart, L. Oliveira, A. Oliveira Sr., D. Ferreira Sr., N. Tamura Sr., A. Shimono, "SUBARU prime focus spectrograph integration and performance at LAM," Proc. SPIE 10702, Ground-based and Airborne Instrumentation for Astronomy VII, 1070288 (12 July 2018); doi: 10.1117/12.2313610

**SPIE.**

Event: SPIE Astronomical Telescopes + Instrumentation, 2018, Austin, Texas, United States

# SUBARU prime focus spectrograph integration and performance at LAM

F. Madec <sup>\*a</sup>, S. Pascal <sup>a</sup>, A. Le Fur <sup>a</sup>, D. Le Mignant <sup>a</sup>, K. Dohlen <sup>a</sup>, R. Barrette <sup>a</sup>, M. Belhadi <sup>a</sup>, S. Smee <sup>b</sup>, J. Gunn <sup>d</sup>, J. Le Merrer <sup>a</sup>, M. Llored <sup>a</sup>, M. Jaquet <sup>a</sup>, P. Balard <sup>a</sup>, P. Blanchard <sup>a</sup>, F. Roman <sup>a</sup>, V. Lapere <sup>f</sup>, JF Gabriel <sup>f</sup>, C. Loomis <sup>d</sup>, M. Golebiowski <sup>b</sup>, M. Hart <sup>b</sup>, L. Oliveira <sup>e</sup>, A. Oliveira <sup>e</sup>, D. Ferreira <sup>e</sup>, N. Tamura <sup>c</sup>, A. Shimono <sup>c</sup>

<sup>a</sup> Aix Marseille Université - CNRS, LAM (Laboratoire d'Astrophysique de Marseille), UMR 7326, 13388, Marseille, France

<sup>b</sup> Department of Physics and Astronomy, Johns Hopkins University, Baltimore, MD, USA 21218;

<sup>c</sup> Kalvi Institute for the Physics and Mathematics of the Universe (WPI), University of Tokyo, Japan  
<sup>d</sup> Princeton University, Princeton, NJ, USA 08544

<sup>e</sup> MCT/LNA –Laboratório Nacional de Astrofísica, Itajubá - MG - Brazil

<sup>f</sup>. Winlight System - France

## ABSTRACT

The Prime Focus Spectrograph (PFS) of the Subaru Measurement of Images and Redshifts (SuMIRe) project for Subaru telescope includes four identical spectrograph modules fed by 600 fibers each. This paper presents the integration, alignment and test procedures for the first spectrograph module composed by an optical entrance unit that creates a collimated beam and distributes the light to three channels, two visible and one near infrared. In particular, we present the performance of the single Red channel module. Firstly, we report on the measured optical performance: optical quality and ghost analysis. We also report on the thermal performance of the visible camera cryostat. Finally, we describe the software used to control and monitor the instrument.

**Keywords:** SUBARU, PFS, SuMIRe, integration, test, fibers spectrograph

## 1. INTRODUCTION

The Prime Focus Spectrograph (PFS) instrument of the Subaru Measurement of Images and Redshifts (SuMIRe) project is presented in Tamura et al<sup>1</sup>. This paper focuses on the assembly, integration and testing of the Spectrograph System (hereafter SpS) for PFS. The SpS design was described in Pascal et al<sup>2</sup> and Madec et al<sup>3</sup>. We summarized here the key-features: SpS includes four identical spectrograph modules (hereafter SM, from 1 to 4) fed by 600 fibers each. Each spectrograph module comprises three optical channels: “blue” (380 to 650), “red” (630 to 970 nm) and “near infrared” (930 to 1260 nm) with a resolving power  $R=2000$  to  $R=4000$ . In addition, the red channel is equipped with an exchange mechanism for the dispersive optics enabling a higher  $R \geq 5000$  spectral resolution.

The SpS is a joint-development including an industrial partner Winlight System in France responsible for delivering the main opto-mechanical assemblies for the spectrograph modules, including the red and blue cameras. Johns Hopkins University and Princeton University are delivering the 4 red and 4 blue visible cryostats, their control electronics and the visible focal planes<sup>4,5</sup> as well as the complete NIR cryostat units. The 4 fiber cable assemblies are developed by Laboratório Nacional de Astrofísica (LNA), Brazil (C. de Oliveira et al.)<sup>6,7</sup>. The Laboratoire d'Astrophysique de Marseille (LAM) is responsible for the assembly, integration, testing and verification (hereafter AIT-V or AIT) of the four spectrograph module in France before shipping each of them, in a sequence, to Subaru.

In parallel of developing the individual components and sub-systems, the international team developed a “one-channel red – visible - spectrograph”, very representative of the full spectrograph module, to test and verify the thermal, mechanical and optical performance. This effort has proven to be extremely useful (beyond expectations!), and lasted

roughly 18 months, much longer than expected. This paper reports on the integration and optical alignment of the one-channel spectrograph (Section 2) and presents the excellent results for the optical performance (Section 3). The thermal performance for the visible camera is covered in Section 4: the thermal performance issues we discovered along the week- or month-long testing sequences, the diagnostic and the thermal model we developed, the changes that were implemented and their associated tests and results. The instrument control software for SpS developed for the AIT phase and the operations is presented in Section 5. Finally, we provide a status update for the on-going AIT for SM1 (three channels) at LAM and present the overall schedule for SpS. We then conclude this technical paper in Section 6.

## 2. INTEGRATION AND OPTICAL ALIGNMENT

### 2.1 Integration

All the components received from consortium or industrial partners are integrated and tested at LAM, see Madec SPIE 2016<sup>3</sup>. Overall dimension of each components mounted on the Carbon Fiber Reinforced Plastic (CFRP) is large, superior to 80cm height and the mass is more than 50kg up to 350kg, so a special care was taken during design phase to securely handle them during installation on the bench. They are also connected to the bench using the precise repositionable interface based on spherulinder, an accuracy lower than 10microns is achieved.

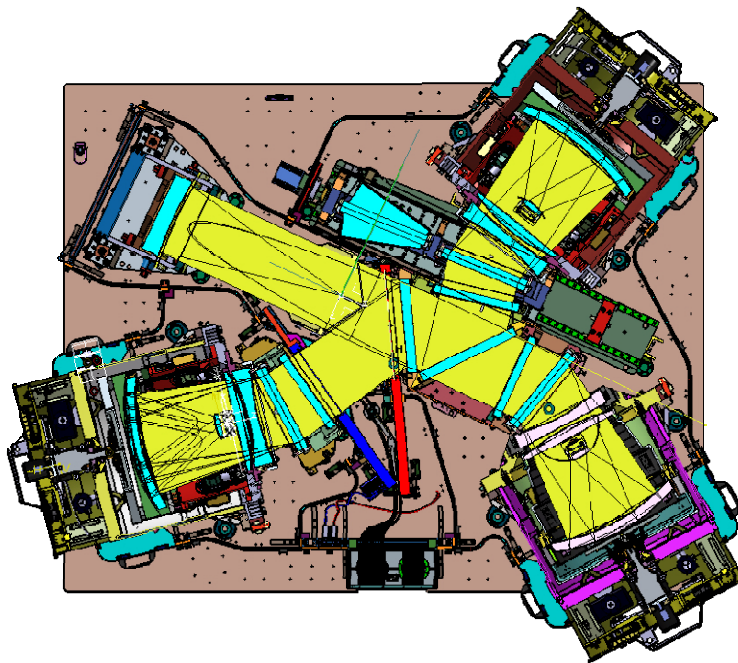


Figure 1. Spectrograph Module cross section.

### 2.2 Optical alignment

Our industrial partner, Winlight System pre-align the optics of the entrance unit and align the correctors, mangin mirror and field lens of the two visible cameras. At LAM we install and align the Fiber Slit Assembly with respect to the collimator mirror. This alignment is made in two main phases; complete sequence is detailed in Figure 2 left. Centration, tip/tilt is done using a reference tool and an alignment telescope see Figure 2 right. Then focus is adjusted using an external reference collimator and a folding mirror placed on an hexapod to select a given fiber of the slit.

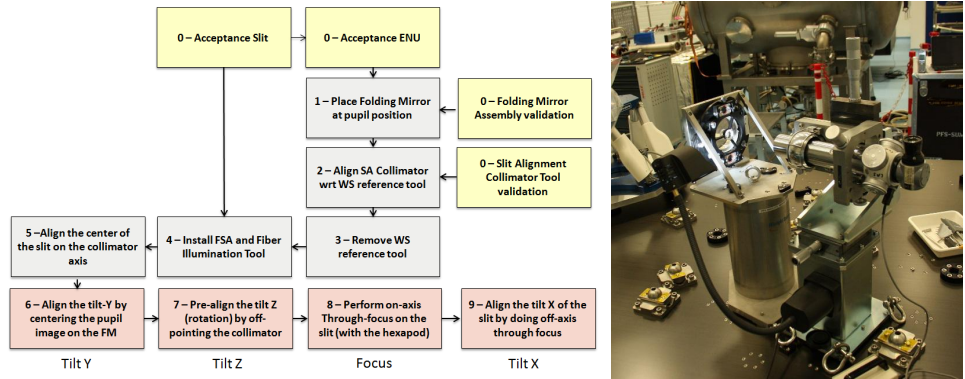


Figure 2 Left: Slit alignment sequence. Right: Optical reference tool and Micro-Alignment Telescope

After slit alignment completion and the dismount of the tools from the bench, we can do the integration of the components. We can thus adjust the roll of the Camera Unit and of the grating then adjust the tip/tilt of the Camera Unit and finally adjust the focus and tip tilt of the Focal Plane Assembly.

The grating roll setting corresponds to the angle between the bottom and top lines of spectrum obtained using a central fiber illuminated by an Hg-Ar spectral lamp.

The vertical tilt of the camera verification is either done using a single wavelength obtain by filtering the Hg-Ar spectral source to illuminate 10 fibers along the focal plane and the position for each fibers is compared to the zemax model, shift of the spectra corresponds to the tilt angle of the camera.

The Focal Plane alignment is based on the throughfocus method

We use the Hg-Ar arc lamp to illuminate 10 fibers. We have identified a list of peaks which are not saturated, with a correct shape, with no neighborhood peak too close (>50pix), localized on the full detector surface area.

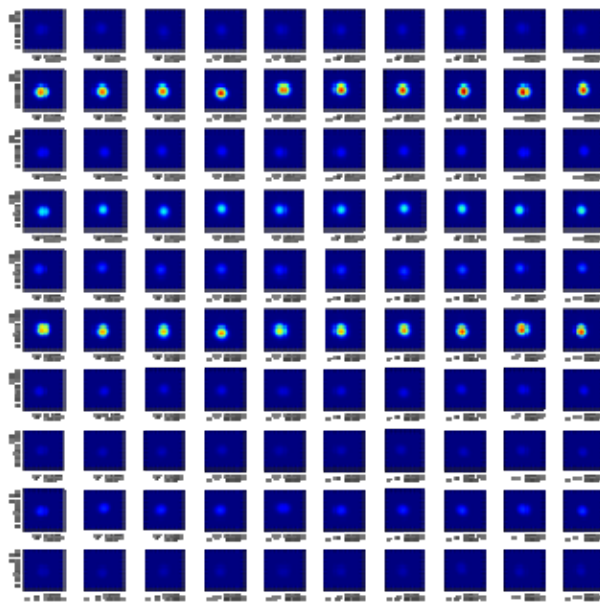


Figure 3 Rois list of all peaks used (peaks are defocused, same scale)

To find the best focal plane we perform through focus, so for each position and for each peak we fit a 2D Gaussian that gives us the centroid, fwhm and amplitude thus ensquared energy in 3 by 3 (EE3) pixels and 5 by 5 pixels (EE5) are calculated.

Then for each peak the best focus position is calculated by finding the maximum of the fit of the EE3 as shown below.

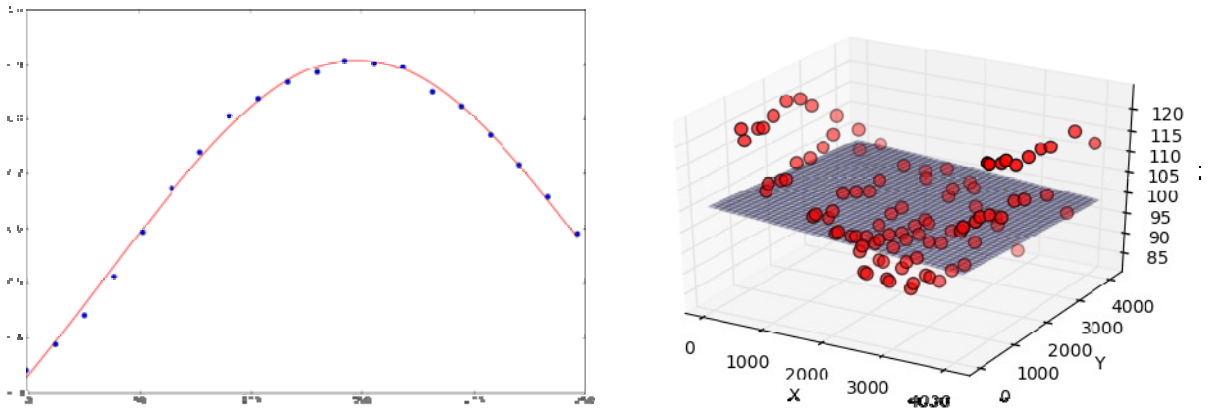


Figure 4 Left: Example of gaussian fit of EE5 for one peak. Right: Best focus plane fit

To move each motors at its position given by the best focus plane fit we need to find the interaction matrix of the focus motors system. For this, we make four different through focus, three starting with a tilt of one motor and one without any tilt.

For each through focus we found the best plane coefficients that become the matrix, we than invert the matrix to find the interaction matrix that allow us to find the wanted motors position.

### 3. SINGLE RED CHANNEL OPTICAL PERFORMANCE

#### 3.1 Requirements overview

The main points concerning optical performance of the one channel spectrograph are image quality and ghosts. These points are addressed by the following requirements:

- Image quality

The Ensquared Energy (EE) for a spatial element (fiber) shall be as listed below:

- $\geq 50\%$  within a square of 3 pixels for each spectral band in more than 95% of the detector area;
- $\geq 90\%$  within a square of 5 pixels for each spectral band in more than 95% of the detector area;

- Ghost requirement:

For a monochromatic image of a single fiber:

- For any in-focus ghost, the total flux per PSF shall be smaller than 0.5% of that of the primary image
- For any out-of-focus ghost, the intensity ratio (maximum ratio of the flux per pixel in the ghost to the flux in the real image) shall be smaller than  $10^{-4}$  for any out-of-focus ghost (with area larger than 1000 pixels).

### 3.2 Image quality

The image quality was measured using a set of different fibers distributed on the whole detector and three different spectral lamps that give spectral lines in the one channel spectral range [650 – 930 nm]. We measured the ensquared energy for all the points on the detector. The image quality obtained was within the specifications and conforms to what was expected considering the manufacturing errors of some optical components (grating in particular).

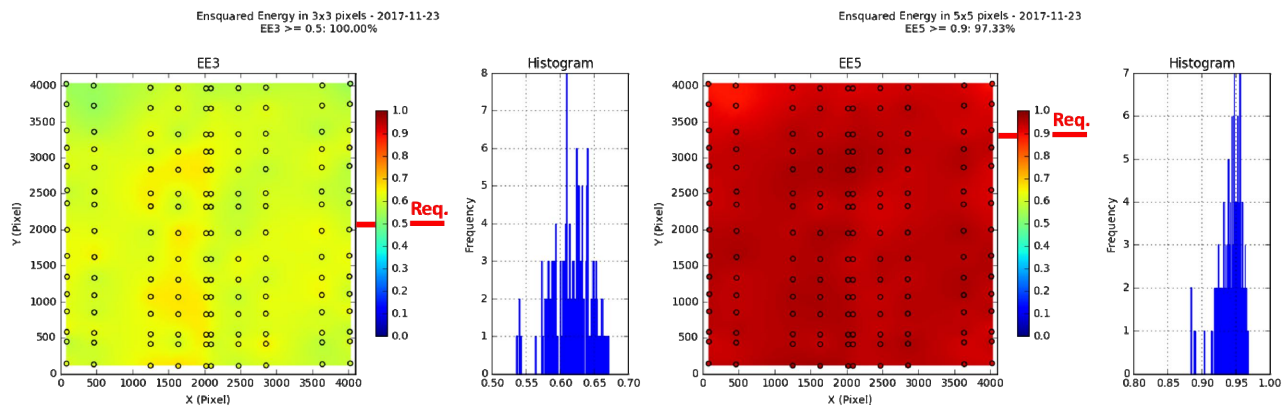


Figure 5 Extended Energy in 3 by 3 (Left) and 5 by 5 (right) pixels measured on the detector (circle represents the fibers used for the measurement)

### 3.3 Ghosts

A main issue of the one channel first images was about ghosts and straylight: In the first images of the spectrograph, we observed some unexpected source of light in the detector. Two main contributions were identified for this straylight contamination:

The first one is the ghosts due to reflection on the detector spiders. The wide FoV and large aperture of the camera leads to rays with almost grazing incidence on the spider arms of the detector. The direct reflection of these rays on these mechanical parts results in ghosts on the detector (see fig). To reduce these ghosts, we decided to modify the spider arms, improving the black coating and mechanical structure of the spider arms to prevent the reflection on these surface. Precisely, a groove structure was added to the spider arms side and detector box and painted with PU1. In return, these modifications lead to a small increase of the spider obscuration.

The second source of straylight identified was due to the optical coders of the slit hexapod, indeed, the entrance slit is set on an hexapod to provide dithering capabilities, the light coming from the optical coders of the hexapod (wavelength 950 nm) result in a diffuse halo on the detector which take about the quarter of the detector area (see fig). Turning off the hexapod power for image acquisition allowed to confirm and remove this source of straylight.

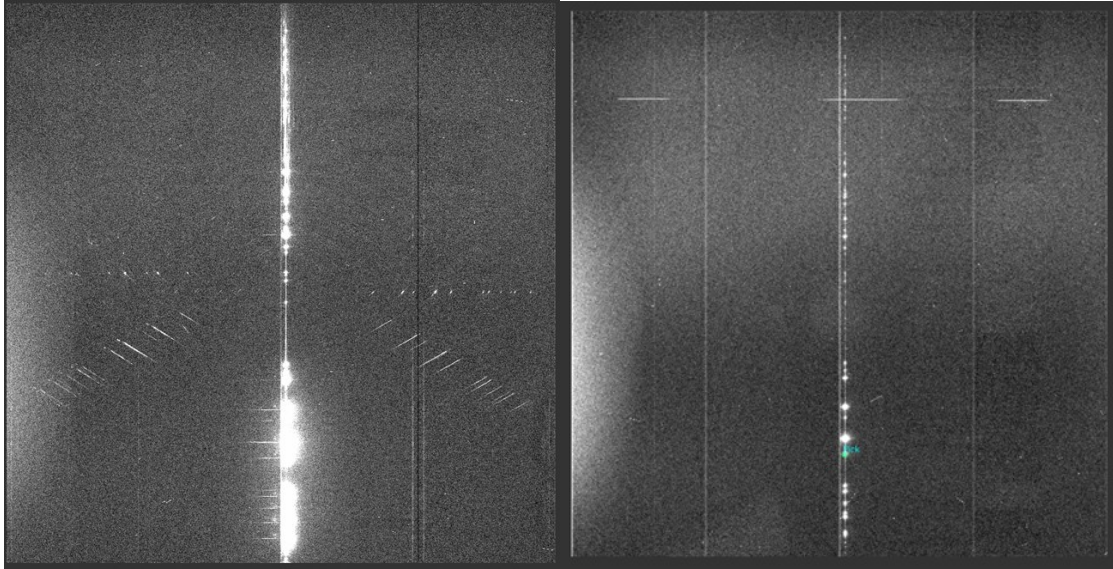


Figure 6 Ghosts due to the reflection on the spider arms and detector box (left) and straylight coming from the hexapod optical coder ( right)

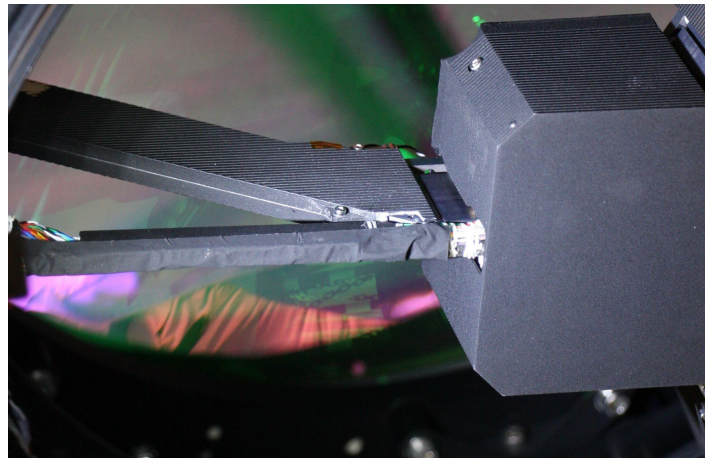


Figure 7 Groove structure added to the spider arms

After these two modifications, the ghosts and straylight level observed on the detector was consistent with expected values.

### 3.4 Conclusion

The “One-channel” allowed us to validate the alignment and the tests procedures. The optical performance obtained full-fill the requirements, in particular the image quality that is the main driver for the spectrograph.

## 4. VISIBLE CAMERA THERMAL PERFORMANCE

### 4.1 Thermal design

The primary function of the visible camera cryostats is to maintain the detectors at their operating temperature of 153K. Contrary to the infrared cryostats, we do not have thermal emissivity issues, so all opto-mechanical parts inside cryostat are maintained warm. As seen in Figure 8 left, cooling power is provided by a cryo-cooler mounted at the back of the cryostat. The cold finger is connected to a thermal spreader plate via copper braids. Three aluminum bars run along the

cryostat body and link to the spiders holding the detector via another set of copper braids and copper rods. These rods, mounted inside a complex structure including an insulating fiber glass (G11) tube and thermal expansion-compensating parts, ensure connection between the warm structure, the cold spiders, and the cooling chain. The mechanical surfaces of all the parts of the cooling chain are polished or covered by aluminized Mylar in order to minimize their thermal emissivity, and warm surfaces facing them are similarly treated.

Due to the complexity of this instrument and its trans-continental work-package breakdown, complete validation of the cryostat system, provided by JHU, could only be done after its mating with the camera opto-mechanics, provided by Winlight, at LAM, see Figure 8 right. In spite of successful individual tests of each unit, we discovered a serious deficiency of the thermal performance of the system at that point. We here describe briefly the various steps that led us to achievement of thermal validation.

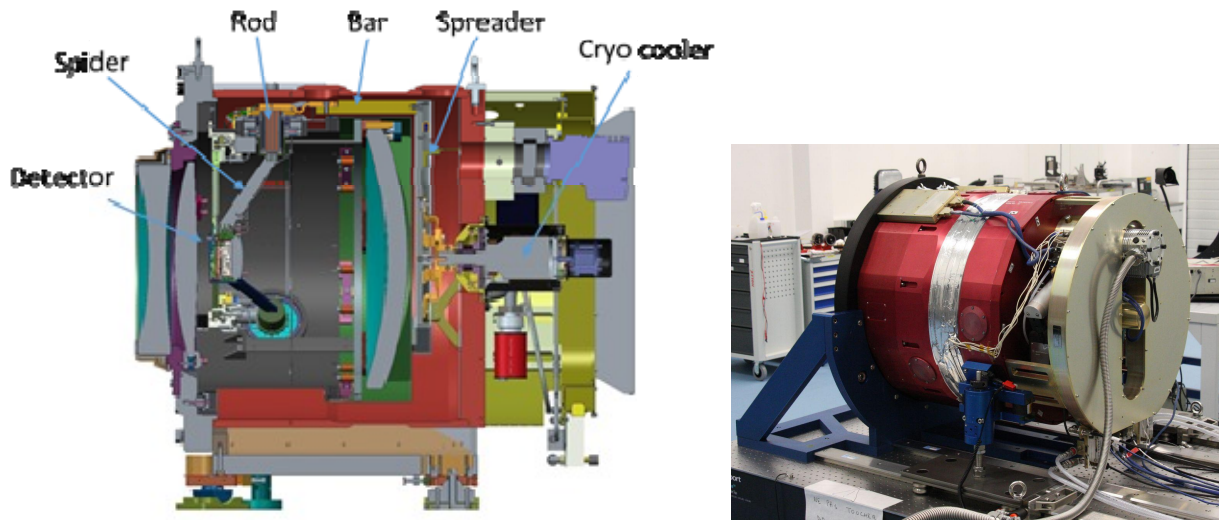


**Figure 8. Left: Cut through the visible camera unit indicating the parts in the detector cooling thermal chain. Right: The thermal validation unit in the lab.**

#### 4.2 Identification of the cryo condensation issue

Initial tests of the system, after preliminary debugging of some basic interface difficulties, showed that while the cryo cooler set-point temperature of 100K was initially reached, the electrical power required to maintain it was larger than expected from the end-to-end thermal model and quickly rising, see Figure 9. This was identified as being due to water vapor out diffusing from the warm mechanical parts condensing onto the cold parts in the cooling chain. Ross [10] gave an excellent review of the physics of cryo condensation, providing the clues to understanding our difficulties. In particular, he showed that in the pressure and temperature range of interest for us, water is the only significantly cryo-condensing gas species, see Figure 10 left. He also showed that cryo-condensed water has high emissivity, increasing strongly with thickness of the ice layer and reaching 90% for 20 $\mu$ m thickness. To counter this effect, several improvement paths were followed. As an immediate action, the cryostat body was baked out, heated up to 60 degrees Celsius for a week while constantly pumping. At the following cooling cycle, both minimum power and drift rate were significantly reduced. At a more fundamental level, the design of the warm parts was scrutinized, identifying in particular the need for improved ventilation of the inner camera cavity. The material list was also studied deeply, revealing notably that black anodization, which is an efficient trap of water vapor, should be replaced by vacuum class black paint (PU1). Some of these improvements were rapidly implemented, leading to further significant improvements.

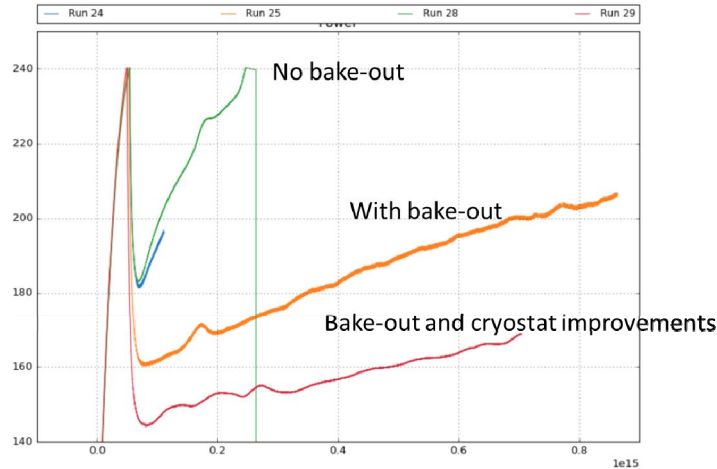


Figure 9. Plots of electrical power consumed by the cryo cooler during three different test runs.

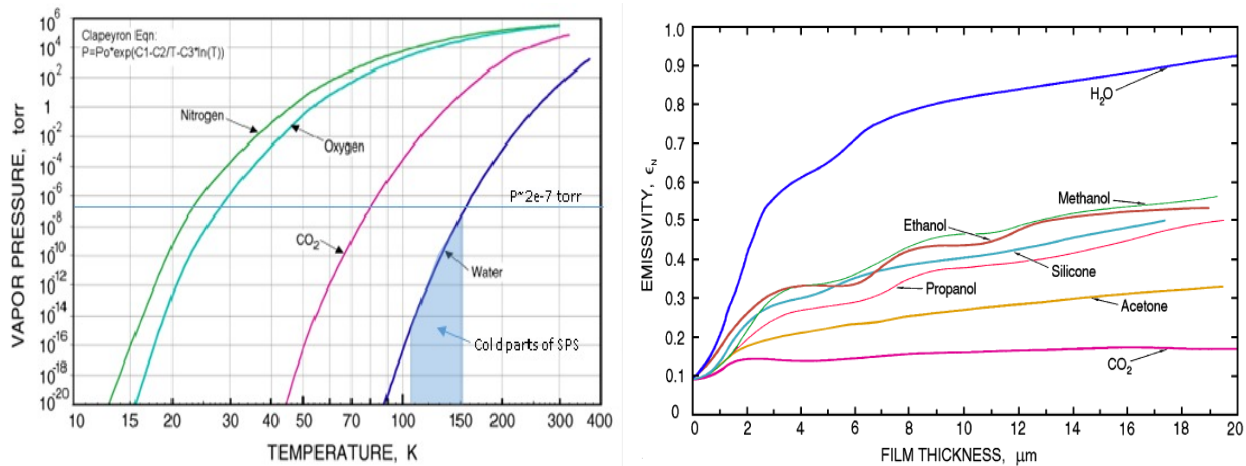


Figure 10. Cryogenic properties for various gas species. Left: Vapour pressure as function of temperature. Right: Emissivity of ices as function of film thickness. Adapted from [10].

### 4.3 Simplified instrument model

A simple thermal model of the camera unit proved an efficient tool to understanding this system. Illustrated in Figure 11, this model considers two temperature levels, warm and cold, ignoring gradients between these levels. The two levels are in radiative and conductive contact. The radiative contact varies in time due to condensation of out-diffused water vapor. Mathematically, this model leads to the following expression for thermal flux:

$$F = C(T_{Warm} - T_{Cold}) + \epsilon \sigma_B A (T_{Warm}^4 - T_{Cold}^4)$$

where  $C$  is conductivity,  $\epsilon$  and  $A$  are emissivity and surface area of the cold elements,  $\sigma_B$  is Stefan-Boltzmann constant,  $T_{Warm}$  and  $T_{Cold}$  are warm and cold temperatures, respectively. Conductivity, assumed constant, was estimated by performing a change in cryo-cooler set point by around 10K. The subsequent change in thermal power allows determining the conductivity to good precision since the fourth power of the cold temperature in the second term is negligible. Using telemetry data, allowing estimation of thermal flux from cryo-cooler electrical power and cold finger temperature using an empirical formula determined during cryo-cooler tests, the emissivity can be calculated.

Emissivity increases at a rate proportional to the out-diffusion rate, expected to fall off exponentially as the warm surfaces gradually deplete. This behavior was indeed observed, with a time constant of about 20 days at room temperature. However, during a run lasting six months, a linear component to the drift was also observed. The exact cause of this component was not fully determined, but possible explanations include external leaks, internal leaks to a trapped air pocket, or the existence of an out diffusing source with very long time constant.

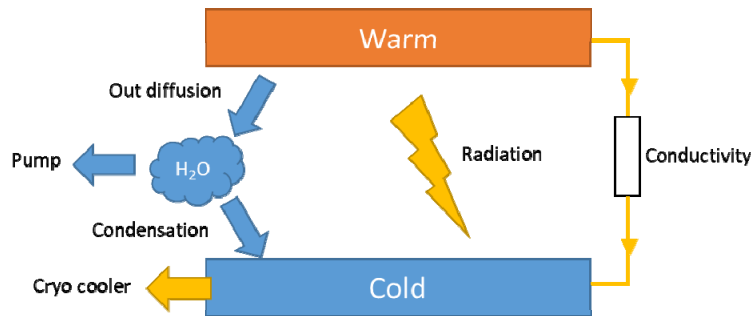


**Figure 11. Simple thermal model of the camera unit illustrating the three mechanisms explaining the thermal performance of the camera unit: out diffusion and condensation, radiation and conduction.**

The following expression for emissivity was used:

$$\varepsilon = \varepsilon_0(t) + at$$

where  $\varepsilon_0(t)$  is the exponentially varying component and  $a$  is the slope of the linear component. The exponential component was calculated using the following incremental expression:

$$\varepsilon_0(t + \Delta t) = \varepsilon_0(t) + \Delta t d\varepsilon/dt$$

with

$$d\varepsilon/dt = (\varepsilon_{Lim} - \varepsilon) \frac{\exp(-E_B/kT_{Warm})}{\exp(-E_B/kT_{20})} \frac{1}{\tau_{20}}$$

where  $\varepsilon_{Lim}$  is emissivity after all water has out-diffused and in the absence of the linear component,  $\tau_{20}$  is time constant at standard room temperature,  $T_{20}=20\text{degC}$  and  $E_B$  is binding energy, allowing determination of the time constant at other temperatures.

This emissivity model was fitted by least squares minimization (Microsoft XL solver) to the emissivity estimated from the telemetry data, see Figure 12. The fit is very good, indicating a binding energy represented by  $E_B/k$  of 10700K, a value compatible with that reported by Inayoshi et al [11], an intrinsic emissivity of  $\sim 4.5\%$  and a limiting emissivity of  $\sim 8.5\%$ , a room-temperature time constant of 20 days and a linear emissivity increase of  $0.47\%/month$ . Note that estimation of binding energy requires data to be taken at different ambient temperatures. For this we arranged for the air-condition in the assembly hall to be decreased by 3 degrees for a couple of days in September and increased by 5 degrees for almost a week end of October, as can be observed on the  $T_{Warm}$  plot, light blue curve, right-hand axis in Figure 12.

During this long run, we also tested a procedure for regenerating the cryostat by boiling off the condensed water. This was done early October as is clearly seen in Figure 12. While this procedure successfully recovered the performance of the cryostat, and even though we recorded increased pressure at the turbo-pump outlet indicating that water was indeed extracted from the cryostat during this process, our secret hopes of recovering a cryostat with less drift following this procedure were disappointed. We suspect the reason for this to be that the largely depleted warm surfaces would suck up released water vapor with greater efficiency than the turbo pump, leaving most of the water inside the cryostat. Still, the operation was successful, allowing us to validate this as a regular maintenance operation.

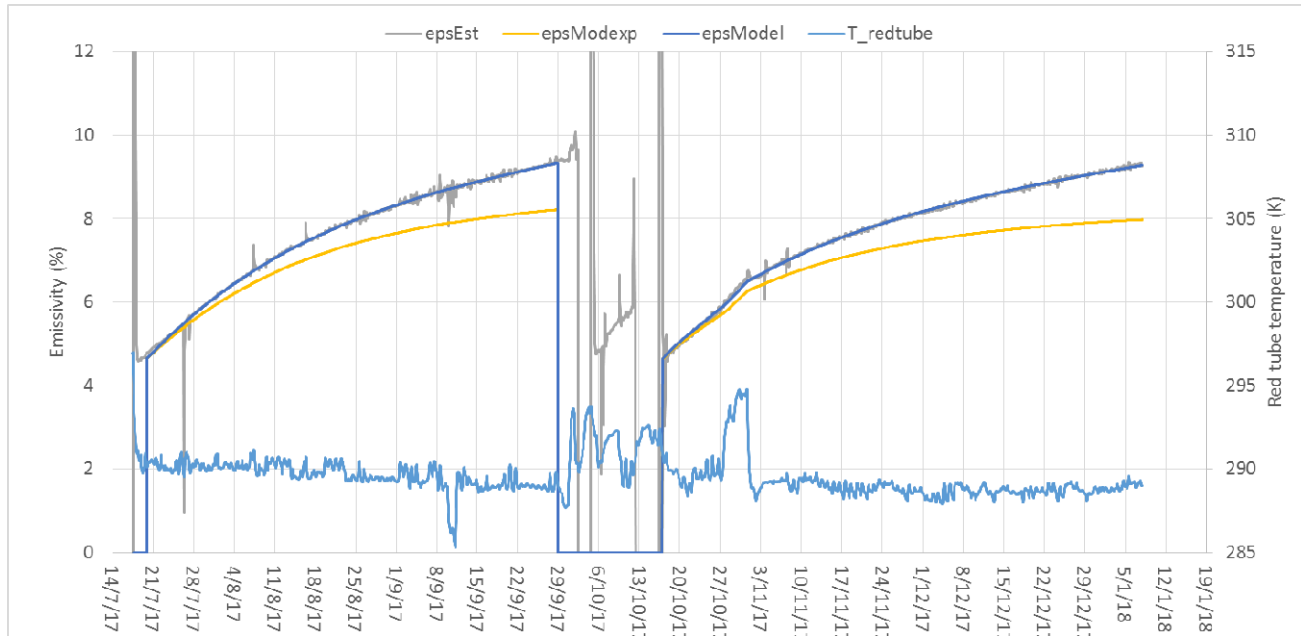


**Figure 12. Emissivity estimated from telemetry data (grey curve) and the fitted model (blue curve). The yellow curve excludes the linear term, illustrating its importance. The event seen early October was a demonstration of the regeneration or boil-off procedure.**

#### 4.4 Cold validation and operation

To further validate the drift model, a cold volume was created around the thermal cryostat in the form of a purpose-built cold chamber (see Figure 13). The goal of this test was to obtain a realistic estimate of the lifetime of the cryostat before requiring regeneration. Predictions using the model indicated that at  $T_{\text{warm}} = 5\text{degC}$ , the exponential drift should be nearly negligible, but the unknown origin of the linear component lead to an uncertainty that only such a cold test could alleviate.



**Figure 13. The thermal validation camera unit inside the cold chamber.**

The cold test was pursued for two months, see Figure 14. Excluding a period of a few days around 24/2, showing a behavior that has not been explained, but whose practical implication is negligible, the fit to the model is very good, see Figure 15. Note also the good stability of the ambient temperature, plotted against the right-hand axis.

The model fit, maintaining the binding energy estimated above, shows an intrinsic emissivity of 3.8% and a limiting emissivity of ~8.4%. The room-temperature time constant remains 20 days, corresponding to a 100-day time constant at 5 degrees, and the linear emissivity increase, now dominating the drift, is 0.33%/month.

These results are fully coherent with those found during the warm tests. The amount of water stored in the cryostat is identical as indicated by the limiting emissivity, but takes much longer to be extracted. The only notable difference in the fit parameters is the linear drift component which has been reduced by a factor  $0.33/0.47 = 0.70$ . The significance of this change is not obvious. If this linear drift is due to a very slow out-gassing component, then it would be expected to fall by a factor 5. If a leak was responsible, then, for constant humidity, it would be expected to be constant. We note, however, that cooler air holds less humidity for a given relative humidity value. Although we have not yet studied this point quantitatively, this would appear as the most probable explanation for the linear drift.

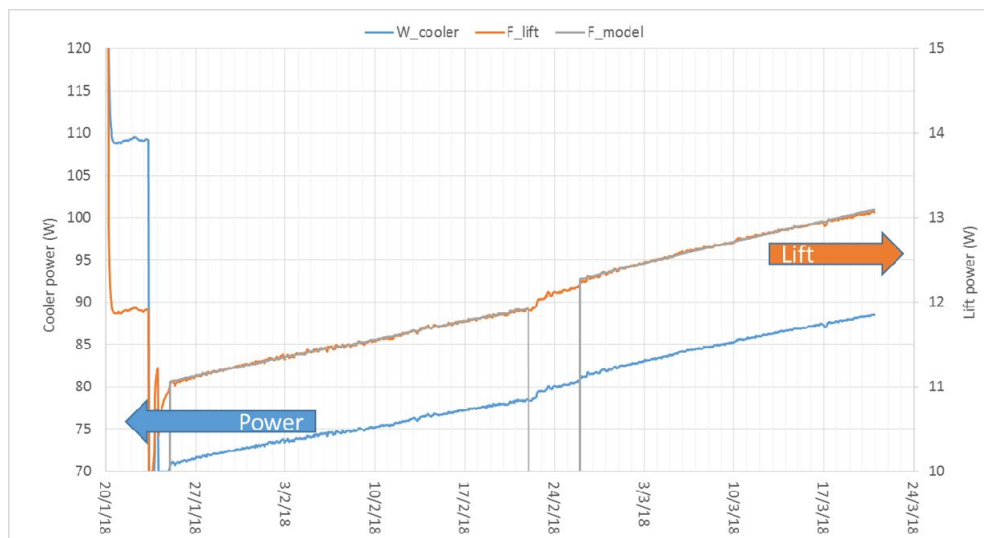
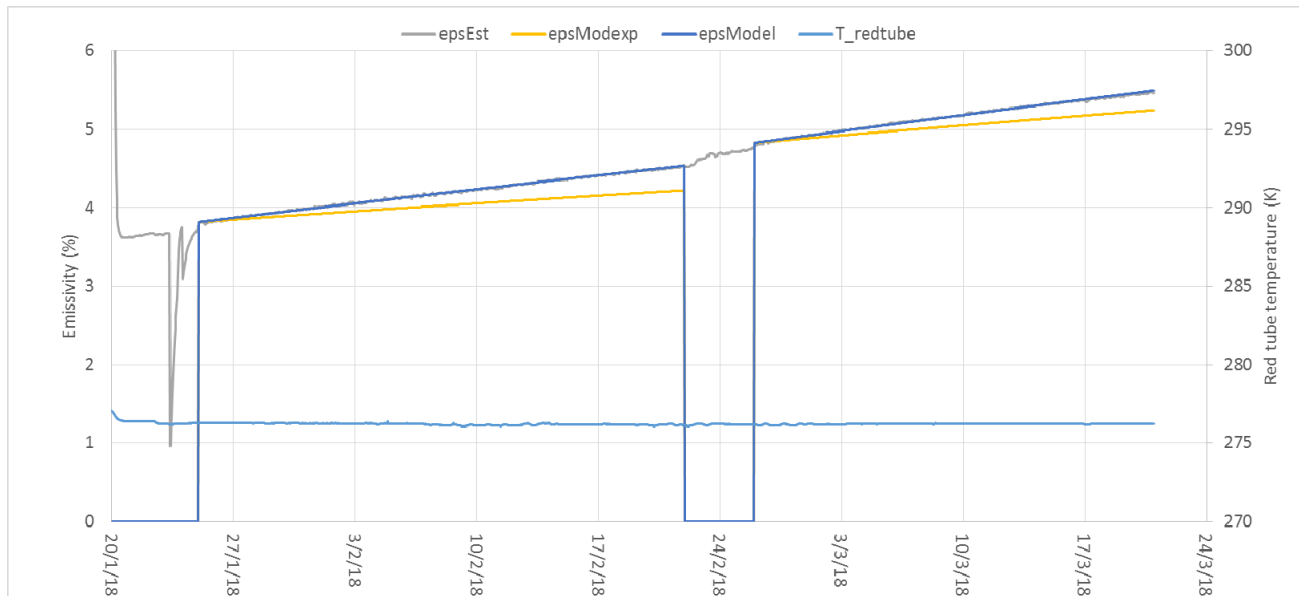


Figure 14. Electrical power (blue curve, left-hand axis) and estimated lift power during the cold run.



**Figure 15.** Same as Figure 12 for the run within the cold chamber, at 5 degC ambient temperature. Note the perfectly stable temperature of the warm part (light blue curve, right-hand axis). The event seen around 24/2 is a “mystery event whose origin has not been explained, but whose practical implication is negligible.

#### 4.5 Conclusion

While early thermal tests were deceiving, good understanding of the system was built up during the test and validation runs. Significant improvements to the system were made and a bake-out procedure implemented, allowing to reach acceptable performance. Elaboration of a model allowed prediction of hold time for thermal performance exceeding 1 year of operation in the cold (5degC) environment at the telescope, and this was confirmed by a final validation run operated in a cold chamber.

Still, this limited hold time does impose maintenance operations to regenerate the cryostats. This operation, which will take a few days involves letting the cryostat warm up while pumping. It can be finely scheduled based on the actual power telemetry profile and to profit from full-moon periods when the instrument’s main science goals are inaccessible.

## 5. SOFTWARE

### 5.1 Instrument Control Software

#### 5.1.1 Architecture overview

In the instrument, each device is handled and controlled by a high level programming structure called Actor. They follow a well-defined structure where some functionalities (command handling, network protocols, etc ...) are already implemented. They are designed to encourage independent and parallel development of hardware and software subsystems, and their eventual integration. Furthermore, this factorized approach also greatly improves testing and maintenance, by making hardware more directly accessible.

These actors are connected to a central hub machine called MHS (Messaging Hub System) which runs a service called “Tron”.

Tron is a relatively simple distributed communication system using twisted, an event-driven network programming framework written in Python and licensed under the MIT License.

The very basic principle, shown in figure below, is that tron central hub accepts commands received from *commanders* (client, actors ...) and dispatches them to actors. They will reply to commands and generate status keywords, also via the hub. As a consequence, the only significant requirement is that each component or program must come with a published dictionary describing status keywords which fully define the state of the module, and that in operation those keywords are kept updated. Moreover, an archiver service track and store these keywords in a PostgreSQL database.

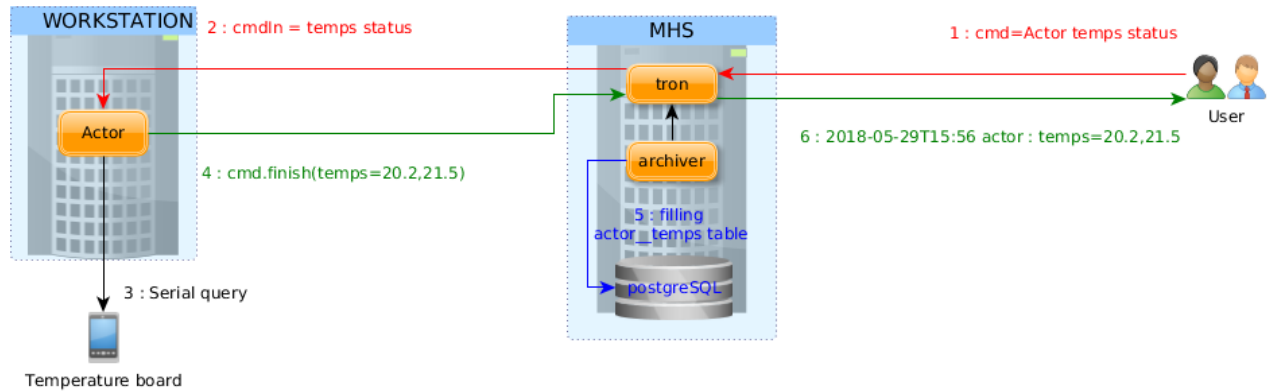


Figure 16 MHS Software

### 5.1.2 Entrance unit overview

For the control software of the Entrance Unit, the enuActor has been built on top of the Actor library.

It control several assemblies such as :

- IIS : Internal Illumination Sources
- BIA : Back-Illumination Assembly
- FSA : Fiber Slit Assembly mounted on its hexapod
- RDA : Red Dispenser Assembly
- SHA : Shutter Assembly
- ENU : Environment (Temperature, humidity)

However, some functionalities common to all devices have been added:

Each device can be simulated and consequently all the commands are still available even if the hardware is not connected.

They rely on finite-state machine, which prevents a misuse of the device and helps operator to diagnose any failure.

All devices are controlled in parallel thanks to a dedicated thread.

### 5.2 Acquisition and control tools

For the optical alignments and the one-channel acceptance, we need in addition a software that will coordinates all actors and allow the user to control and monitor the one-channel.

Since we have actors with a dedicated purpose running in different places, we need a super-Actor or sequencer which, thanks to single command generate a list of commands and dispatches them sequentially.

That's why, we have developed ics\_spsaitActor which allows us to perform sequences within the spectrograph environment. This sequencer has several available commands : take an exposure, or perform some through-focus etc ...

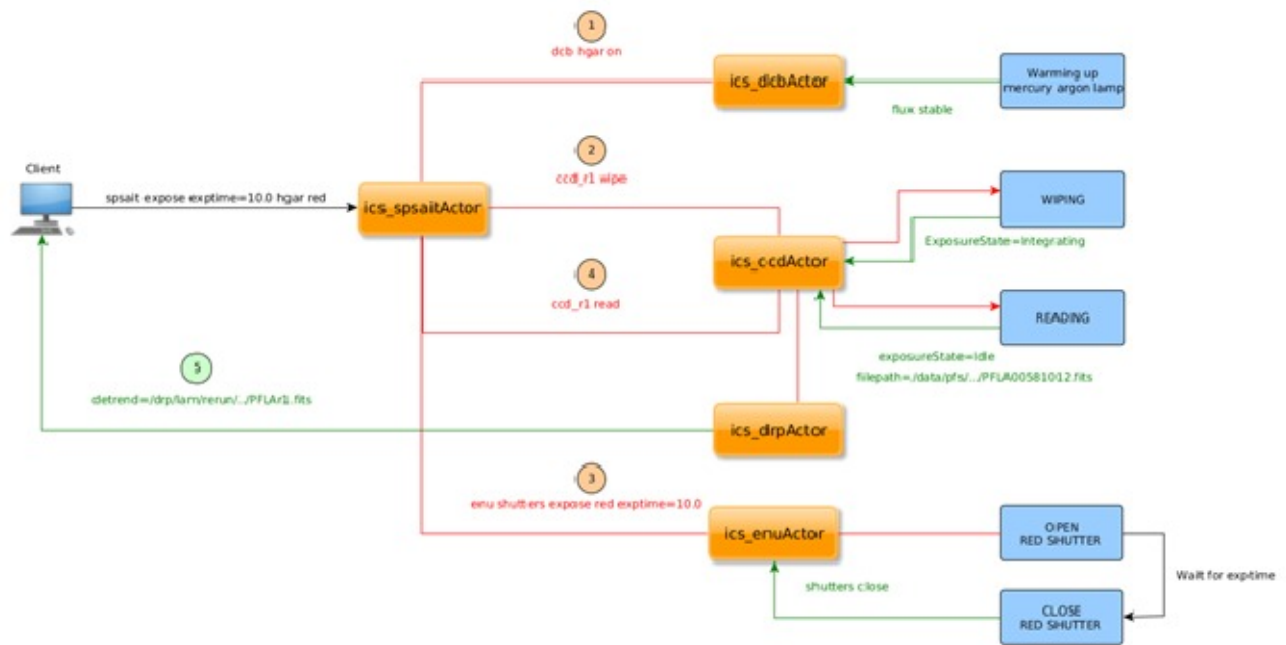


Figure 17 : Arc lamp exposure sequence

Moreover, to control and monitor sps one channel devices, a Graphical User Interface has been developed. This interface includes a sequence manager which allows the user to plan several acquisition sequences in advance and launch them automatically during nighttime.

Each sequence is systematically logged, it contains information gathered from the system and fields added by the operator. As a result, we know the goal, parameters of each sequence, and the file(s) path of the matching data can be easily retrieved. This feature has revealed to be particularly useful for data processing.

We are using Ginga9 to display the 4k\*2k detector images. This astronomical data viewer is written and maintained by software engineers at the Subaru Telescope.

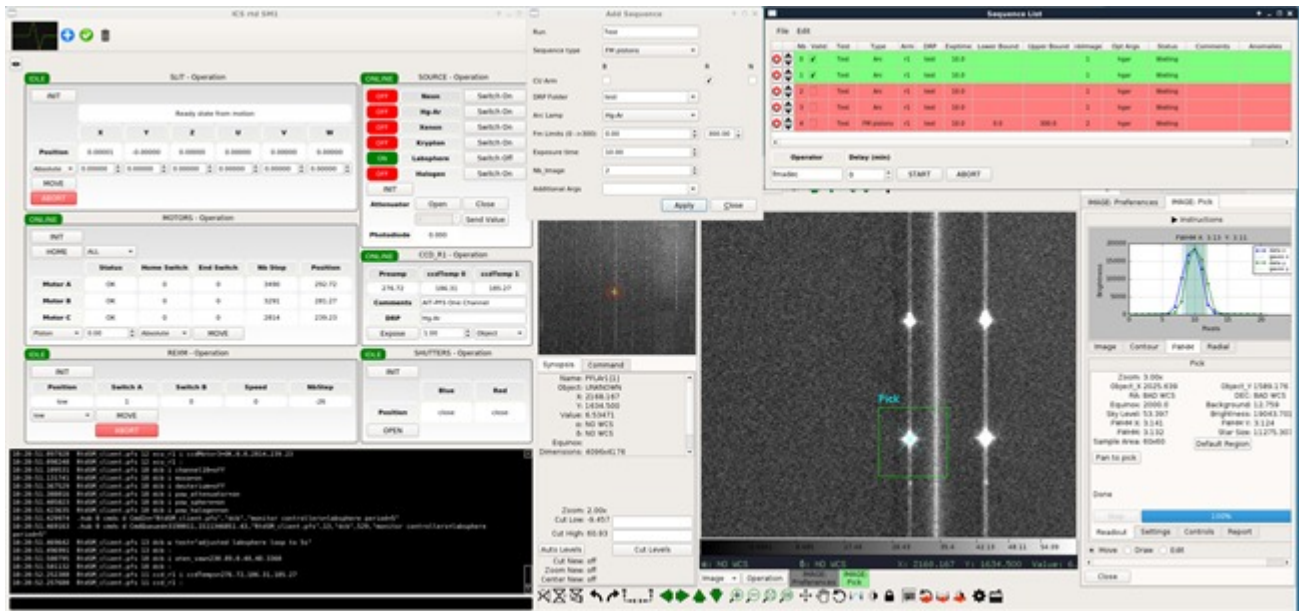


Figure 18 One-channel instrument control and image viewer GUI

### 5.3 Monitoring and alarm tools

Personnel and instrument safety is a top priority during AIT Phases.

It is required to develop monitoring and alarm handling tools to answer our needs:

*plotData* is a flexible tool which allows you to plot data and custom your figures. It' has been made to be both a real time monitoring software and data display. We use it to monitor pressure, temperature sensors ...

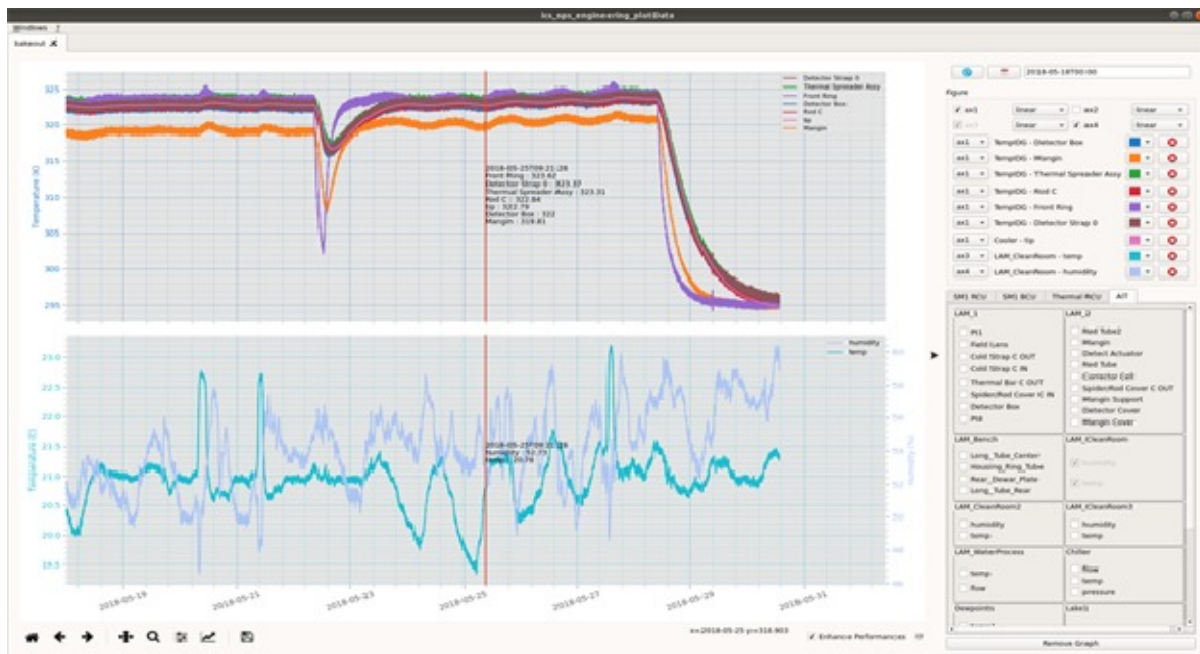


Figure 19 PlotData window

monitorData is a monitoring tools which gives a global view of all Camera unit status.

As some devices are critical, we have added some visual alarms when they reach an unexpected state.

They are defined in different configuration file for each operation mode (pumpdown, cooldown, nominal).

We switch from one mode to the other following AIT operation.

PfsBot is using XMPP protocol, it can be reached by any xmpp chatting client.

It's instantiated for each camera, it allow us to get status from camera devices, but also to handle and receive alarms.

Additional features has been added such as generating dataset or pdf report and share it by email

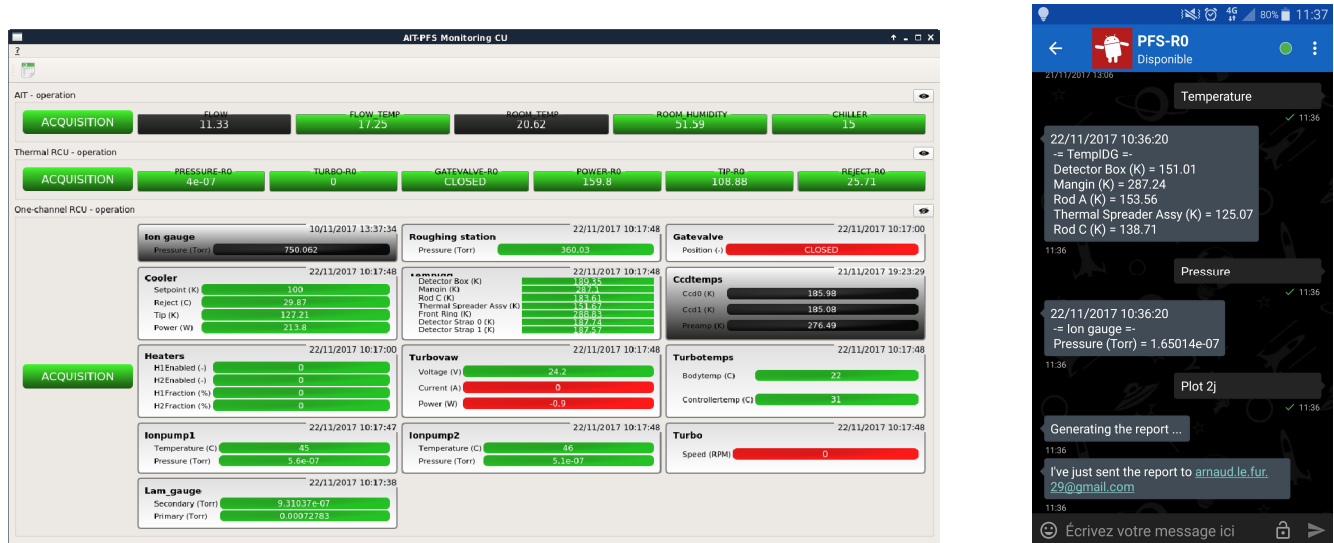


Figure 20 Left: MonitorData window. Right: Jabber bot client

## 6. CONCLUSION

The “one-channel” developed in parallel of the rest of the spectrograph was a real opportunity not only to demonstrate the performance of the instrument but also to validate all the procedures: optical alignment, optical test, thermal test, and integration process. We also validated the software analysis tools. Even if we have encountered serious issues with the thermal performance of the visible cameras, we succeeded to solve them and finally achieved very good performance. We are now receiving SM1 hardware components with all the improvements implemented and we have completed the assembly of its two visible cameras. Their thermal performances are now even better than expected.

LAM should receive the NIR camera from JHU Baltimore in late October 2018. Then, after a month of tests of the complete spectrograph module, it will be shipped to the SUBARU Telescope for the installation to start beginning of 2019. In parallel, we will start working on SM2 in October 2018, benefiting from the large capacity of LAM’s ISO8 integration hall to fit two full spectrograph modules side by side.

## ACKNOWLEDGEMENT

We gratefully acknowledge support from the Funding Program for World-Leading Innovative R&D on Science and Technology (FIRST) program "Subaru Measurements of Images and Redshifts (SuMIRe)", CSTP, Japan.

This work was also made possible through a contractual agreement within the Subaru PFS consortium between the Max Planck Institut für Astrophysik (Garching, Germany) and the Laboratoire d'Astrophysique de Marseille (CNRS/Aix Marseille University).

## REFERENCES

- [1] Naoyuki Tamura, "Prime focus spectrograph for the Subaru telescope: ongoing integration and future plans" Proc. SPIE 10702-48 (2018).
- [2] Sandrine Pascal, "Optical design of the SuMiRe/PFS spectrograph" Proc. SPIE 9147-158 (2014).
- [3] Fabrice Madec, "SUBARU prime focus spectrograph: integration, testing and performance for the first spectrograph" Proc SPIE 9908-329 (2016).
- [4] Murdock Hart, "Focal plane array alignment and cryogenic surface topography measurements for the Prime Focus spectrograph" Proc SPIE 10709-106 (2018).
- [5] James E. Gunn, "Detector and control system design and performance for the SuMIRe prime focus spectrograph (PFS) cameras" Proc SPIE 9908-338 (2016).
- [6] Antonio C. de Oliveira, "Fiber input assembly for PFS/SUBARU" Proc. SPIE 10702-282 (2018).
- [7] Antonio C. de Oliveira, "FRD characterization in large-scale for FOCCoS PF/SUBARU" Proc. SPIE 10702-283 (2018).
- [8] Stephen A. Smee, "Visible camera cryostat design and performance for the SuMIRe Prime Focus Spectrograph (PFS)" Proc. SPIE 9908-333 (2016).
- [9] Ginga is a Python toolkit for building viewers for astronomical and scientific images stored in numpy data arrays. <http://ejeschke.github.io/ginga/>
- [10] R.G. Ross, Jr., "Cryocooler Load Increase due to External Contamination of Low- $\epsilon$  Cryogenic Surfaces." Presented at the 12th International Cryocooler Conference, Cambridge, MA, June 18-20, 2002.
- [11] Inayoshi et al, 1998